

Experimental Investigation on Deposits of ER70S-6 Wire on SiO₂ Substrate Using Non-Transferred Arc Based Wire Arc Additive Manufacturing

suvranshu pattanayak (✉ suvranshupattanayak@gmail.com)

NIT Rourkela: National Institute of Technology Rourkela <https://orcid.org/0000-0002-7068-7130>

Susanta Kumar Sahoo

Ananda Kumar Sahoo

Research Article

Keywords: WAAM, NTA, GRA, microstructural analysis, dislocation density, residual stress

Posted Date: March 31st, 2022

DOI: <https://doi.org/10.21203/rs.3.rs-1445580/v1>

License:   This work is licensed under a Creative Commons Attribution 4.0 International License. [Read Full License](#)

Abstract

Recent trends in additive manufacturing (AM) are to produce geometrically complex structures at minimal wastage of material, time and cost, without sacrificing part quality, mechanical performance and to introduce ease in processing and part removal. Here a non-transferred arc (NTA) based wire arc additive manufacturing (WAAM) system has been developed to achieve the above objectives, where arc is only generated between tungsten electrode and consumable filler wire. No electrical contact with substrate facilitates deposits even on non-conductive substrate surface that helps in easy removal of final deposits. Influence of deposition parameters (welding current, voltage, wire feed speed (WFS), and travel speed) on response characteristics (bead uniformity, height deviation, droplet diameter, droplet transfer frequency) is studied on multi-performance level using grey relational analysis (GRA). Then single and multi-bead layer is fabricated over SiO_2 substrate for ease in part removal after complete fabrication. WFS is referred as a key deposition parameter which have influence on all deposition characteristics. It has been observed that NTA based WAAM results high bead uniformity with minimal spatter and bead height difference between start and exit arc point. Complete ferrite microstructure with few pearlites is observed on the deposits with similar elemental composition on top, bottom and interface surface. X-ray diffraction (XRD) study reveals ferrite diffraction planes ($\{110\}$, $\{200\}$, $\{211\}$, and $\{220\}$) with no intermetallic formations on deposits. Also, compressive residual stress with less variation in crystallite size, stress, strain and microhardness among top, bottom, and lateral surface of deposit indicates isotropic nature of the fabricated part.

1. Introduction

Wire arc additive manufacturing (WAAM) becomes a promising alternative to powder-based processes because of cleaner environment, reduction in material cost, chances of porosity, contamination, waste and improvements in rate of deposition, utilisation of raw material, part density, cost-effectiveness, process and energy efficiency [1–7]. Gas metal arc welding (GMAW) gains more popularity than gas tungsten arc welding (GTAW) and plasma arc welding (PAW) based WAAM because of improved bonding strength, energy efficiency, rate of metal deposition, mechanical performance, and lower fabrication time [1, 2, 4, 8–12]. But still there are some concerns related to GMAW-AM like, noticeable deviation in bead height between start and exit point of the arc, spatter generation, high heat input, difficulties in part removal from substrate after complete fabrication [2–6]. These limitations are addressed by the development of a NTA system. In NTA approach, the arc is generated between tungsten electrode (attached with the -ve terminal of GMAW power source) and filler wire (attached with the +ve terminal of GMAW power source). Here no electrical connection is made between substrate and electrode. So electrical conductivity of the substrate is not a critical aspect of this approach. Therefore deposition can also be made on non-conductive substrate, which facilitates easy withdrawing of deposits after complete fabrication without any material wastage. This process relies on drop by drop transfer of molten metal to the substrate. Therefore the time for which molten pool retains its liquidity reduces, which promotes faster cooling action than conventional GMAW based WAAM approach. This promotes faster deposition rate as compared to the conventional GMAW based WAAM approach. Also, due to no arc contact with substrate, most of the heat generated at arcing

zone is utilised for melting the wire electrode. Therefore heat input to substrate reduces, whereas deposition efficiency is enhanced.

Few approaches were adopted to get control over bead geometry [3–6]. **Xiong et al.** [3] had proposed an online monitoring (improved neuron self-learning strategy) and control (passive vision sensing system having CCD camera and composite filtering) strategy for saving the material and energy during deposition of H08Mn2Si wire. It was reported that neuron self-learning controller delivers constant bead width with more than 10% material and energy saving by regulating the input process parameters during deposition. The same passive vision system was also adopted to maintain a constant nozzle tip to plate distance (NTPD) during fabrication of single-bead multilayer wall (21 layers) [4]. The precision of this model was found to be ± 0.5 mm. This approach is also used for maintaining bead width as per the NTPD value [5]. **Xiong et al.** [6] had developed another approach to overcome these bead height deviations during fabrication of single beads multilayer having both open and closed paths. Process of alternation in the direction of deposition for each layer helps in regulating height deviation for open-loop structures. For closed loop structures, higher travel speed (TS = 7.5 mm/s) was adopted which goes on decreasing towards exit point of arc (TS = 5 mm/s).

In some longitudinal studies, a subtractive manufacturing approach like milling operation was followed after subsequent depositions to get control over layer thickness. **Song et al.** [10] had developed a 3D welding and milling approach for fabricating a thin wall (consists of 8 layers) of mild steel using AWS 5.18 70S-6 wire (0.9 mm diameter) at a fixed welding condition, i.e. voltage (U) = 19 V; current (I) = 120 A; TS = 1.2 m/min. Milling approach helps in maintaining the uniform layer thickness (from 0.1 mm to 1 mm) and a geometrical accuracy of ± 0.01 mm and ultimate tensile strength (UTS) of 620 MPa was achieved through this approach. In another study, **Song et al.** [11] applied the same strategy to fabricate multiwalled parts using two distinctive deposition strategies. First approach involves manufacturing of square block of 30 layers using AWS5.18 ER308 stainless steel as outer region and AWS5.18 ER70S6 mild steel as inner region. Second approach involves deposition of secondary material (Tin-Bismuth eutetic alloy) within the previously created boundary line of primary material (AWS 5.18 ER 308 stainless steel). No cracks were found at the interface. In an interesting study, **Suryakumar et al.** [12] had adopted a similar strategy to remove scales and scallops forms over bead surface as well as to maintain uniform layer thickness during deposition of ER70S6 wire (0.8 mm diameter).

In an interesting study, canny edge detection method was employed by **Cao et al.** [13] for determining bead geometry and to develop a bead overlapping model for adjacent beads using these datasets. Optimal overlapping percentage was found to be 63.66% for sine function and highest fitting accuracy (fitting error = 0.0179), coefficient of determination and F-values, with reduced volume of valley was achieved. In another remarkable study, **Xiong et al.** [14] implemented three fitting curves (circular, parabola, and cosine) to model the single beads deposited from copper coated mild steel wire (1.2 mm diameter) by robotics GMAW-AM. It was concluded that when the ratio of WFS to TS was higher than 12.5, then parabola bead fitting curve is preferable with a center distance of 6.133 mm. Otherwise, circular arc model was considered with a center distance of 5.242 mm. **Li et al.** [15] adopted a layer overlapping strategy (LOP) during fabrication of multilayered components. The proposed mathematical model also considered the shortage

of material at the edges of deposits. It was reported that the model not only generates flat surfaces but also reduces area shortages in the first bead.

In some remarkable studies, rolling process was adopted for generating flat beads to ensure proper bead overlapping with negligible material overflow [16–18]. **Colegrove et al.** [16] had designed a rolling coupled GMAW based AM. Here slotted (slot depth = 10 mm) as well as a profiled roller (same profile with bead geometry) was used to study its impact on residual stress, distortion and grain size reduction. It was reported that slotted roller was found as effective for reducing residual stress and distortion than profiled roller, also a reduction in grain size was noticed due to the compression of columnar grain under high rolling load. In another longitudinal study, **Xie et al.** [17] adopted a metamorphic rolling mechanism (MRM) at 3000N load on depositions of 304 stainless steel. In MRM, roller profile was selected according to the bead profile of top and lateral surfaces. There was a reduction in height deviation (from 2.4 mm to 0.2 mm) between start, and exit arc point and width deviation (from 0.45 mm to 0.12 mm) is noticed. A similar approach was also adopted by **Dirisu et al.** [18] to investigate the impact of residual stress development on microstructure and mechanical performance of ER70S-6 deposits. It was reported that under high rolling conditions (160 KN), compressive residual stress and flat beads were obtained with uniform cross-section throughout the entire bead. As a result deposition strength (tensile and fatigue) is enhanced due to reduction in stress concentration, crack initiation and propagation possibilities.

GMAW based WAAM approach was also used during the fabrication of functionally graded materials (FGM) using ER70S-6 and ER110S-G wire by **Somashekhara et al.** [19]. Hardness of the final object depends upon hardness of each filler wire. In another longitudinal study, **Abe et al.** [20] deposited Ni6082 wire material over previously deposited YS308L wire. But an intermediate layer was fabricated between them by combining both wires. The chemical composition of intermediate layer was found to be increased with increasing number of layers. In a scientific study, **Liu et al.** [21] determined the impact of deep cryogenic heat treatment duration on microstructure and mechanical strength during fabrication of Cu-Al-Si alloy using ERCuSi28 and ER4043 wire. DCT time of 12h shows increase in UTS and YS by 23.3% and 19.9%, respectively due to further grain refinement.

In an interesting investigation, both GMAW and GTAW are combined to develop a double electrode based GMAW-WAAM (DE-GMAW) [22, 23]. Here a secondary arc (bypass arc) is generated between tungsten and filler wire due to the use of two distinctive machines and corresponding current flow about it, is called bypass current. It reduces the magnitude of current that passes through the base metal and subsequently reduces heat input to substrate. Therefore bead height deviation reduced from 20% and 13% improvements in material utilization was achieved. In recent studies, compulsively constricted WAAM was developed by **Guo et al.** [24] for getting control over excess heat input during deposition. Here arc is generated between tungsten electrode and filler wire (HS211 silicon bronze of 1.2mm diameter). This means there are no electrical connections made with the substrate. The influence of welding current, voltage, and gas flow rate on arc behaviour and droplet transfer process was studied. It was reported that under the high value of welding current and gas flow rate, a high droplet transfer frequency was attained with a small droplet diameter. But in such approaches, arc blow was noticed, which may affect the droplet transfer process. A similar study was also reported in [25, 26] for depositing ER70SG wire of 1.2 mm diameter on a Q235 base

plate. The temperature of ejected plasma increases at a higher value of welding current. In a recent study **Zhou et al.** [27] followed the same procedure to introduce a filler wire into an indirect arc between tungsten electrodes. This approach results in low heat input with no current flow through droplets and molten pools.

Collectively, the above-reported studies outline the application of GMAW based WAAM with some strategies to get control over bead geometry and mechanical strength. Limited works have been incorporated on NTA based WAAM. The primary focus of this investigation is to develop an understanding of NTA based WAAM. Here some single beads are deposited over 8 mm thick mild steel to study the impact of deposition parameters (U, I, TS and WFS) on bead geometry (bead uniformity, difference in the height of bead between start and exit point of arc) and droplet characteristics (diameter and detachment frequency). In order to generate the best deposition parameter GRA approach has been adopted. Under optimum deposition conditions, both single and multilayered deposits are made on SiO₂ substrate for easy withdrawing of deposits. Microstructural, elemental composition, residual stress, and microhardness test are also incorporated to study variation in both top and bottom surface of deposits. XRD study is also conducted for identifying crystallographic phases, crystallite size, lattice strain, and dislocation density on wire, top and bottom surface of the deposits.

2. Materials And Procedures

Pictorial presentation of the NTA based WAAM system is depicted in Fig. 1. In NTA based WAAM, the arc is ignited between tungsten electrode (attached with the -ve terminal of GMAW power source) and wire electrode (attached with the +ve terminal with GMAW power source). Here a tungsten electrode of 3.2mm diameter, and ER70S6 filler wire of 1.2mm diameter is used throughout the experimental trial. The electrode holder and gas supply system is shown in Fig. 2(a). The electrode holder is manufactured from a copper block. The internal gas supply system provides shielding gas coaxially with the tungsten electrode to create a smooth arc and plasma jet. At the same time, an external gas supply is provided just nearer to the ceramic nozzle opening. This design is adopted to facilitate axial detachment of molten droplets (as shown in Fig. 2(b)). The process parameters combination at which experiments are performed is shown in Table 1. Here 99.99% argon gas is used for shielding the arcing zone at a constant flow rate of 10 l/min. Standoff distance between substrate and electrode is kept constant at 8 mm throughout the experiments. A L25 orthogonal array (as shown in Table 2) is designed using the parameters provided in Table 1. To begin with, single beads are deposited over mild steel (8 mm thick) substrate for studying the parametric influence. Then a groove of 10 mm depth is made on SiO₂ substrate to provide a stable base during deposition of multilayered beads under optimum deposition conditions. Bead uniformity (W_d), difference in bead height between start and exit point of arc (H_d), droplet diameter (D), and detachment frequency (f_n) are considered as response characteristics. Bead uniformity represents the standard deviation in bead width. So high bead uniformity reflects a low value of standard deviation. Table 2 represents the response parameter values corresponding to each parameter set. Microhardness, microstructural analysis, XRD, and EDS analysis are performed on the multilayered deposits over SiO₂ substrate.

Table 1
Deposition parameters and their level settings

Deposition Parameters	Unit	L1	L2	L3	L4	L5
Welding voltage (U)	V	18.5	19.0	19.5	20.0	20.5
Welding current (I)	A	65	70	75	80	85
Travel speed (TS)	m/min	0.048	0.096	0.144	0.192	0.240
Wire feed speed (WFS)	m/min	2.5	3.0	3.5	4.0	4.5

Table 2
L25 orthogonal array and measured deposition characteristics

Expt. No.	U (V)	I (A)	TS (m/min)	WFS (m/min)	W _d (mm)	H _d (mm)	D (mm)	f _n (Hz)
1	18.5	65	0.048	2.5	1.0265	0.08	6.77	1.4
2	18.5	70	0.096	3	1.0236	0.13	3.30	2.8
3	18.5	75	0.144	3.5	0.6970	0.74	3.08	3
4	18.5	80	0.192	4	0.6597	0.85	4.12	5.8
5	18.5	85	0.24	4.5	0.5650	0.17	3.31	10.8
6	19	65	0.096	3.5	0.6704	0.21	4.10	5.6
7	19	70	0.144	4	0.7413	0.08	3.41	6.8
8	19	75	0.192	4.5	0.8986	0.24	2.89	12.8
9	19	80	0.24	2.5	1.1788	0.07	6.21	2
10	19	85	0.048	3	1.2690	0.29	5.08	3
11	19.5	65	0.144	4.5	0.6218	0.02	4.41	12.2
12	19.5	70	0.192	2.5	0.9455	1.62	4.50	2.6
13	19.5	75	0.24	3	2.4081	1.31	3.96	3.4
14	19.5	80	0.048	3.5	0.9810	0.01	3.14	6.2
15	19.5	85	0.096	4	0.6593	0.04	3.00	7.4
16	20	65	0.192	3	2.0975	0.51	5.63	2
17	20	70	0.24	3.5	2.0107	0.44	3.54	3.4
18	20	75	0.048	4	0.3828	0.04	3.44	7.4
19	20	80	0.096	4.5	0.9433	0.27	3.66	10.8
20	20	85	0.144	2.5	1.8949	0.16	5.73	1.8
21	20.5	65	0.24	4	3.1438	0.58	3.36	6.6
22	20.5	70	0.048	4.5	1.7782	1.81	3.25	13.2
23	20.5	75	0.096	2.5	3.1069	1.28	4.85	1.4
24	20.5	80	0.144	3	3.1983	1.18	4.15	2
25	20.5	85	0.192	3.5	3.1438	0.32	4.23	2.6

3. Statistical Analysis

Statistical analysis is adopted to establish mathematical relationship among input and output characteristics. Here GRA based multi-performance approach is incorporated into the experimental data sets that determines optimal parameter set by collectively considering all response characteristics.

3.1. Grey relational analysis

The procedure followed during execution of GRA approach are discussed below [28, 29].

Step 1

Data pre-processing is followed to make a comparison among the response attributes, as the unit of measurement of responses differs from one another (Table 3).

Step 2

Deviation sequence is determined (Table 3).

Step 3

Deviation sequence is utilised for grey coefficient determination for all quality characteristics. Finally, grey grade is generated by taking the average of grey coefficients for each experimental trial (Table 4).

Step 4

Graphically represent the experiment sets with their grey grades (see Fig. 3(a)) for ease in determination of optimized deposition condition.

Step 5

Preparation of response table (see Table 5) and graph (see Fig. 3(b)) for ease in determination of the best factor level setting.

Step 6

A confirmation test is performed based on the parameter settings obtained from Table 5.

Table 3
Data pre-processing and deviation sequence

Expt. No.	Data pre-processing				Deviation sequence			
	W_d	H_d	D	f_n	$\Delta_{01}(k)$	$\Delta_{02}(k)$	$\Delta_{03}(k)$	$\Delta_{04}(k)$
1	0.7724	0.9611	0	0	0.2276	0.0389	1	1
2	0.7749	0.9333	0.8931	0.1186	0.2251	0.0667	0.1069	0.8814
3	0.8884	0.5944	0.9503	0.1356	0.1116	0.4056	0.0497	0.8644
4	0.9016	0.5333	0.6816	0.3729	0.0984	0.4667	0.3184	0.6271
5	0.9353	0.9111	0.8916	0.7966	0.0647	0.0889	0.1084	0.2034
6	0.8978	0.8889	0.6868	0.3559	0.1022	0.1111	0.3132	0.6441
7	0.8727	0.9611	0.8660	0.4576	0.1273	0.0389	0.1340	0.5424
8	0.8168	0.8722	1	0.9661	0.1832	0.1278	0	0.0339
9	0.7173	0.9667	0.1449	0.0508	0.2827	0.0333	0.8551	0.9492
10	0.6852	0.8444	0.4338	0.1356	0.3148	0.1556	0.5662	0.8644
11	0.9151	0.9944	0.6085	0.9153	0.0849	0.0056	0.3915	0.0847
12	0.8001	0.1056	0.5856	0.1017	0.1999	0.8944	0.4144	0.8983
13	0.2806	0.2778	0.7229	0.1695	0.7194	0.7222	0.2771	0.8305
14	0.7875	1	0.9348	0.4068	0.2125	0	0.0652	0.5932
15	0.9018	0.9833	0.9709	0.5085	0.0982	0.0167	0.0291	0.4915
16	0.3910	0.7222	0.2940	0.0508	0.6090	0.2778	0.7060	0.9492
17	0.4218	0.7611	0.8307	0.1695	0.5782	0.2389	0.1693	0.8305
18	1	0.9833	0.8581	0.5085	0	0.0167	0.1419	0.4915
19	0.8009	0.8556	0.8020	0.7966	0.1991	0.1444	0.1980	0.2034
20	0.4630	0.9167	0.2671	0.0339	0.5370	0.0833	0.7329	0.9661
21	0.0194	0.6833	0.8789	0.4407	0.9806	0.3167	0.1211	0.5593
22	0.5044	0	0.9065	1	0.4956	1	0.0935	0
23	0.0325	0.2944	0.4952	0	0.9675	0.7056	0.5048	1
24	0	0.3500	0.6733	0.0508	1	0.6500	0.3267	0.9492
25	0.0194	0.8278	0.6547	0.1017	0.9806	0.1722	0.3453	0.8983

Table 4
Grey relational coefficients and grade

Expt. No.	$\zeta_i (1)$	$\zeta_i (2)$	$\zeta_i (3)$	$\zeta_i (4)$	Grey Grade	Order
1	0.687189	0.927835	0.333333333	0.333333333	0.5704226	15
2	0.689584	0.882353	0.823832943	0.36196319	0.6894333	9
3	0.817539	0.552147	0.909564932	0.366459627	0.6614277	12
4	0.835629	0.517241	0.610911649	0.443609023	0.6018477	13
5	0.885383	0.849057	0.821799033	0.710843373	0.8167705	2
6	0.830352	0.818182	0.614866096	0.437037037	0.6751092	10
7	0.797036	0.927835	0.78870363	0.479674797	0.7483125	7
8	0.731855	0.79646	1	0.936507937	0.8662059	1
9	0.638795	0.9375	0.368980449	0.34502924	0.5725762	14
10	0.613669	0.762712	0.468959559	0.366459627	0.5529501	18
11	0.854886	0.989011	0.560858068	0.855072464	0.8149569	3
12	0.714414	0.358566	0.54682822	0.357575758	0.494346	21
13	0.410053	0.409091	0.643439889	0.375796178	0.4595951	23
14	0.701783	1	0.884625466	0.457364341	0.7609431	6
15	0.835809	0.967742	0.944975348	0.504273504	0.8132	4
16	0.450847	0.642857	0.414605877	0.34502924	0.4633348	22
17	0.463738	0.676692	0.747062277	0.375796178	0.5658221	16
18	1	0.967742	0.778916699	0.504273504	0.812733	5
19	0.715244	0.775862	0.716374404	0.710843373	0.729581	8
20	0.482137	0.857143	0.405562144	0.341040462	0.5214706	19
21	0.337694	0.612245	0.804958858	0.472	0.5567244	17
22	0.502203	0.333333	0.842440554	1	0.6694943	11
23	0.340707	0.414747	0.497624863	0.333333333	0.396603	25
24	0.333333	0.434783	0.604849549	0.34502924	0.4294987	24
25	0.33769	0.743802	0.591502932	0.357575758	0.5076425	20

Table 5
Response table

Parameters	Level-1	Level-2	Level-3	Level-4	Level-5	Max-Min	Ranking
Welding Voltage (V)	0.6679	0.6830	0.6686	0.6185	0.5119	0.1711	2
Welding Current (A)	0.6161	0.6334	0.6393	0.6188	0.6424	0.0263	4
TS (m/min)	0.6733	0.6607	0.6351	0.5866	0.5943	0.0867	3
WFS (m/min)	0.5110	0.5189	0.6341	0.7065	0.7794	0.2684	1

4. Results And Discussion

Twenty-five single beads are deposited over mild steel substrate (as shown in Fig. 4) at different parameter combinations as single beads have maximum influence over the geometrical accuracy of multilayered deposits.

The interrelation between comparative and reference sequences becomes stronger when a high grey relational grade value is achieved by the experiment set. Therefore from Table 4 and Fig. 3(a), it has been recognised that **experiment number-8** is the optimised parameter set. Again to determine the significance of different deposition parameter level values on entire response characteristics and their ranking, a response table (Table 5) and graph (Fig. 3(b)) has been prepared. Response table and graph is prepared by taking the average of grey relational grade values conforming to each parameter level. The maximum grey grade value for each process parameter level represents the optimal condition at which better control over response characteristics is achieved. As per the above explanation, 'A₂, B₅, C₁, D₅' is the best parametric condition and at this setting a confirmation test (as shown in Table 6) is performed and its response characteristics are compared as with **experiment number-8**. It also conforms from Table 5 that WFS has maximum control over bead geometry and droplet transfer behaviour followed by welding voltage, TS and current. Therefore WFS is termed as a key deposition parameter during multi-criteria analysis.

Table 6
Confirmation test at 'A₂, B₅, C₁, and D₅' parametric combination

Symbol	Deposition Parameters	Deposition Characteristics
A	Welding voltage (U) = 19.0 V	Bead width deviation (W _d) = 0.1849 mm
B	Welding current (I) = 85 A	Height deviation (H _d) = 0.15 mm
C	Travel speed (TS) = 0.048 m/min	Droplet diameter (D) = 2.61 mm
D	Wire feed speed (WFS) = 4.5 m/min	Droplet detachment frequency (f _n) = 13.6 Hz

Better performance characteristics are obtained from the confirmation test as compared to initial experiment (**experiment number-8**). It is due to the enhancement in welding current value, which improves heat generation at the arcing point that leads to proper melting of wire electrode and generates less droplet

diameter with higher detachment frequency. Similarly, under low TS, droplets are properly deposited on the substrate surface and give rise to low bead width and height deviation. The process of droplet transfer at 'A₂, B₅, C₁, and D₅' parametric combination is depicted in Fig. 5 (a-f). It describes all phases of droplet transfer like its generation (Fig. 5 (a)), path of movement (Fig. 5 (b-e)), and final deposit (Fig. 5 (f)) on the metal surface. Now at 'A₂, B₅, C₁, and D₅' parametric combination single (Fig. 6 (a)) and multilayered deposits (Fig. 6 (b)) are prepared over SiO₂ substrate for ease in part removal after complete deposition.

4.1. Parametric influence on bead width deviation

The influence and percentage contribution of deposition parameters on a particular response attribute is determined from the ANOVA analysis (as shown in Table 7). For a definite response characteristic, the percentage contribution of deposition parameters is determined by taking the ratio between Adj. SS. values for the deposition parameters to the total Adj. SS. conform to that response attribute.

Table 7
Adj. SS. values of deposition parameters for different deposition characteristics

Deposition parameter	Adj SS for W _d	Adj SS for H _d	Adj. SS for D	Adj. SS for f _n
Welding voltage (U)	14.0795	2.2836	1.2517	9.344
Welding current (I)	0.1763	1.4526	5.3791	1.216
Travel speed (TS)	1.6997	0.3172	0.9388	4.272
Wire feed speed (WFS)	3.4208	0.5573	16.8746	333.952
Total SS	19.3763	4.6107	24.4442	348.784

It has been recognised that bead width deviation is highly controlled by welding voltage followed by WFS, TS, and current. To study the variation of bead width deviation with deposition parameters, few graphical representations are prepared (as shown in Fig. 7 and Fig. 8). It has been observed that under high welding voltage, the bead width deviation increases. Thermal energy generated at the arcing zone depends upon voltage drop and current density [2, 13, 30, 31]. Current flow through electrons and ions is constant, so heat generation varies with respect to the voltage drop at two electrodes [30, 31]. As reported by Cao et al. [13], under high voltage, thermal energy generation becomes more which enhances the melting rate and droplet detachment. It also aggravates the plasma force and generates an unstable plasma jet. Under high voltage, arc length between two electrode increases. Therefore droplet forms at wire tip is highly oscillating between the inter-electrode gaps due to unstable stable plasma jet. So the droplets continuously come in contact with the tungsten electrode and give rise to high tungsten diffusion and wear (as shown in Fig. 9 (a-h)). In such a case percentage of tungsten in the deposits increases. When tungsten starts to diffuse, the arc plasma starts oscillating from left to right at a high velocity; therefore, no consistency was achieved in the droplet transfer process [24–27]. This results in poor bead uniformity (high deviation).

Similarly, under a higher value of WFS, the deviation in bead width was found to be reduced. High WFS raises the arc current, which enhances the heat input and magnitude of electromagnetic pinch force at the

wire tip [2, 12, 14, 32]. Therefore molten droplets (of small size) are detached at a faster rate rather than oscillating at wire tip. Therefore the chance of contact of molten droplet at tungsten side reduces that results uniform bead. So WFS must be set to higher values at high welding voltage for producing fine and uniform beads. TS symbolises the speed at which worktable moves. TS basically maintains heat input and deposition per unit length [33–37]. For a definite value of welding voltage, current and WFS, the droplet detachment frequency is constant. So when table moves faster (TS is more), then the droplets do not adhere properly to the substrate and gives rise to poor bead uniformity and reduces the geometrical accuracy of the form part [25].

4.2. Parametric influence on bead height deviation

ANOVA analysis (from Table 7) convey that welding voltage and current are the most crucial deposition parameters that affect the difference in bead height between start and exit point of arc. To study the variation of bead height difference with deposition parameters, few graphical representations are prepared (see Fig. 7 and Fig. 10). It has been recognised that under the high value of welding voltage, height deviation increases due to unstable metal transfer results from unstable plasma jet [24–27]. Heat generation at arcing zone is determined from the product of welding voltage and current [2, 12, 13, 30, 31]. Therefore at higher current and voltage, the heat generation is aggravated [38–41], also heat content of the plasma jet increases [25]. As the process goes on, temperature of substrate increases and results in a reduction of thermal gradient, which retains the deposits in molten state for longer duration of time due to reduction in viscosity of molten pool under high temperature [2]. Therefore the flowability of molten metal is enhanced that gives rise to high bead width at low height towards exit point of arc as a result adequate difference in bead height is noticed [2, 6, 24–27, 41].

It has been noticed from Fig. 7 that height deviation is raised with a rise in TS, but it again reduces after a certain limit of TS [5, 6, 12, 14]. Under the high value of current and voltage, the plasma jet temperature increases [25]. The interaction time between plasma jet and substrate reduces upon increase in TS that reduces the heat input [26, 33–39, 42]. So the substrate temperature is not increasing so rapidly, which enhances the temperature gradient and promotes faster solidification [12]. Therefore the deposits are solidified quickly rather than free-flowing, which gives rise to a reduction in height difference between start and exit point of the arc. Under high WFS, an excessive amount of wire get melted and deposited over the substrate, so the chance of difference in the height of bead reduces [43, 44]. In general, better control over height deviation is achieved in the NTA approach compared to GMAW based WAAM.

4.3. Parametric influence on droplet diameter

Droplet diameter is highly controlled by WFS followed by welding current and voltage (observed from Table 7). The dependence of droplet diameter with deposition parameters is presented in Fig. 11–12. It is noticed that under the low magnitude of welding current, the droplet diameter is increasing. The magnitude of electromagnetic pinch force is directly related to the squared value of current [2, 24–27, 32]. So under a low level of current, the magnitude of pinch force is curtailed, and surface tension force is increased [45]. Therefore instead of detachment, its diameter continuously increases. But due to the increase in droplet

diameter and reduction in surface tension force, the droplet starts oscillating under the action of buoyancy and promotes the arc between droplet and tungsten electrode. So the arc and plasma jet starts oscillating due to the oscillation of droplet. As a result, consistency in droplet transfer was not achieved. Therefore droplet comes in frequent contact with tungsten electrode at high droplet diameter, which aggravates the tungsten diffusion and wears. The adhesion of droplets on tungsten electrode raises the iron content on tungsten side, which is evident from the EDS analysis (see Fig. 13). The EDS report of tungsten electrode (wt% of different elements) after depositing a bead under a low level of current is presented in Table 8.

A sharp fall in droplet diameter is noticed upon increasing the WFS. High WFS promotes a high flow of arc current between two electrodes, which generates high thermal energies at arcing zone [2, 12, 14]. That helps in generation of concentric plasma jet (as shown in Fig. 14) and effective melting of wire electrode. Therefore droplet diameter reduces at high temperature [25]. Also at high temperature, the surface tension force decreases [45]. As a result, the droplet is not able to retain at the wire tip for a longer duration of time. Therefore droplet detachment occurred at a faster rate with a reduction in diameter.

Table 8
Wt% of elements present on tungsten electrode surface at a low level of welding current

Element	Fe	W	Th
Wt%	48.49	50.97	0.54

4.4. Parametric influence on droplet detachment frequency

ANOVA analysis (from Table 7) convey that WFS is the key deposition parameter that affects the droplet detachment frequency most, whereas other parameters have negligible impact. High WFS conduct maximum arc current that produces high amount of heat energy at arc spot [2, 3, 14]. It also enhances the magnitude of electromagnetic pinch force at wire tip [2, 32]. Electromagnetic force pinches the droplet at wire tip that helps in detachment of droplets. Also, due to high-temperature generation, the surface tension force is diminished at the wire electrode tip that prevents the long duration adherence of droplet at wire tip and promoting faster detachment [45]. Therefore under high WFS, droplet detachment frequency is enhanced (as shown in Fig. 11 and Fig. 15). Arc length between tungsten and wire electrode depends upon the value of welding voltage. Small voltage results a small confined arc length. Therefore there is less space available for the growth of droplets between two electrodes. So the droplets continuously come in contact with the tungsten electrode and leads to a reduction in droplet detachment frequency and aggravates the tungsten wear (as shown in Fig. 9). But upon increasing the welding voltage, space available between two electrodes increases, which promotes free detachment of droplets without colliding with tungsten electrode. But after a certain limit with the increase in welding voltage, the droplet transfer rate reduces. As very high welding voltage generates an unstable arc that promotes high plasma oscillation, in such case, droplet again starts oscillating and makes frequent contact with tungsten electrode. That reduces the droplet transfer rate with increased chances of tungsten wear.

There also exist another factor (argon gas flow rate) that have some effects on droplet transfer rate. To study the impact of gas flow rate on droplet transfer frequency, depositions are made under different gas flow rate settings, but other parameters remain same as with the confirmation test. It is noticed from Fig. 16 that with a hike in gas flow rate, the droplet transfer rate increases. As it again enhances the plasma temperature, that leads to higher melting of wire electrode. As a result, droplet diameter reduces with high detachment frequency [24]. Under a very high gas flow rate (22–26 l/min), the plasma jet velocity increased rapidly that makes unstable droplet transfer due to the reduction in droplet size. In absence of shielding gas, the tungsten electrode wear and diffusion is aggravated. Also, powders of yellowish in colour are formed on the tungsten electrode surface under the absence of shielding gas, as oxygen reacts with tungsten and forms tungsten oxide, which is determined under EDS analysis (as shown in Fig. 17). During some practices, a 2.4 mm tungsten electrode is also used for studying the influence of electrode diameter on droplet transfer behaviour. It is observed that when the gas flow rate is more than 22 l/min, in such case tungsten electrode starts to burn. But at a gas flow rate of 26 l/min, the tungsten electrode bends after some time due to higher localised heat concentration under high plasma temperature. Application of argon gas for shielding also assists in maintaining the geometrical accuracy of the fabricated part [46].

4.5. Microstructural analysis

Microstructural analysis is performed on the multilayered deposited over SiO_2 substrate. After deposition, small blocks are cut from the top, bottom, and interface between two adjacent beads through wire electrical discharge machining (WEDM). Specimen preparation is the most crucial aspect for microstructural analysis. All three samples undergo grinding (using a belt grinder) to produce a flat surface. Then polished with emery paper (1/0, 2/0, 3/0, and 4/0) and Al_2O_3 paste (through cloth polishing) to generate a scratch-free mirror-like surface. Finally, etchant (nital solution (4% HNO_3 and 96% $\text{C}_2\text{H}_5\text{OH}$)) is used to remove the non-metallic inclusions and impurities present on the sample surface and to reveal phases and grain boundary. Now the specimens are observed under a Scanning electron microscope (SEM) to identify the different phases. Microstructure of the top, bottom, and interface zone is depicted in Fig. 18(a-f). The enlarged view of microstructure is presented in Fig. 18 (d-f).

In all the micrographs, complete ferrite colonies are observed with few pearlite phases (volume fraction is low with respect to ferrite phase). The ferrite that formed is known as proeutectoid ferrite as it forms before the starting of eutectoid reaction. It is commonly observed in hypo-eutectoid steel. Similar micrographs are obtained during GMAW based WAAM using ER70S6 wire [18, 47, 48]. In Top surface grains (see Fig. 18(a)) are slightly bigger than the bottom surface (see Fig. 18(b)); this could be due to the difference in the rate of cooling between top and bottom surface of the deposits that occurred due to reduced heat dissipation rate in top surface of the deposit with increased number of layers [41]. With respect to top and bottom surfaces, the grain size is quite smaller in the intermediate zone between two layers (as shown in Fig. 18(c)). During depositing a layer, some amount of heat is being transferred to the previously solidified layer [49]. So the previous deposit again undergoes recrystallisation and forms smaller and fine grains as compared to top and bottom layer. Fine pearlites are observed along with coarse pearlite in the top surface and interface layers. Whereas only coarse pearlites are observed in the bottom surface of the deposit. A reduction in size

and enhancement in fineness of pearlite is noticed with increase in layer thickness (with increase in number of layers). This could be due to the reduction in cooling rate in the top and interface which enhances the growth and nucleation rate of pearlite [50]. Also under low cooling rate, the deposits remain at higher temperature for longer duration of time as a result the inter-lamellar spacing between Fe₃C lamellae reduces, which gives rise to the development of fine pearlites [50].

After deposition of a layer, a small droplet is solidified at the wire tip, whose microstructure is depicted in Fig. 19. It also exhibits a similar microstructure as with the deposits. Therefore it can be concluded that the type of microstructure shown in the final fabricated part is completely depends upon cooling characteristics and temperature gradient maintained during the deposition process [51]. The elemental composition at wire, top, bottom, and interface layer is identified through EDS analysis. The element identified on wire, top, bottom, and interface layer is depicted in Fig. 20 and Table 9. It has been observed that iron content is maximum in the deposits; also composition of the deposit is almost same in top, bottom, interface zone and holds good agreement with the wire (ER70S-6) composition.

Table 9
Chemical composition of wire and deposits

Sample	Wt% of elements											
	Si	P	S	V	Ti	Cr	Mn	Fe	Ni	Cu	Zr	W
ER70S6	1.19	0.00	0.03		0.00	0.05	1.73	96.73		0.16	0.10	
Top	0.36		0.11			0.22	0.99	97.67	0.31	0.24		0.10
Bottom	0.33	0.07	0.02		0.04	0.04	1.06	97.63	0.16	0.22		0.43
Interface	0.55			0.06	0.05		0.94	97.67	0.56			0.17

4.6. XRD analysis

XRD analysis is conducted through BRUKER D8-Advance®, which uses Cobalt (K- α radiation wavelength of 0.179 nm) as an X-ray source and a Lynxeye detector. The voltage (35 KV) and current (25 mA) are kept constant during all measurements. The two-theta (2θ) angle range is selected from 30°-126°. At the same time, scan rate and step size are selected as 5°/min and 0.02, respectively. The XRD raw data is analysed through X'Pert High Score software to identify the diffraction planes. Diffraction patterns observed on wire, top and bottom surface is depicted in Fig. 21. The identified diffractions planes are {110}, {200}, {211}, and {220} at 2θ angle of 52.3°, 77.2°, 99.6°, and 123.9° respectively as per the JCPDS pattern [06-0696] [52]. Similar results are also reported in previous studies [18, 47, 48]. In all samples, ferrite colonies are observed. But in wire, few copper peaks like {111} and {200} are identified at 50.3° and 59.2° respectively, which conforms to the JCPDS pattern [03-1005] [53]. Copper is basically shown due to the presence of copper coating on filler wire. But their intensities are very low as compared to the intensities of ferrite peaks. But these copper peaks are not presents in the deposited samples, which indicates that the copper coating is evaporated during the melting of wire under the high arc temperature. Instead of scherrer equation, the

Williamson hall (W-H) plot is adopted for computing crystallite size and lattice strain, as broadening of diffraction peaks (ΔK , nm^{-1}) is defined (EQs. 1) using the effect of both crystallite size and lattice strain [54]. Here a scatter plot is prepared between $4\text{Sin}(\theta)$ (in X-coordinates) and $a\text{Cos}(\theta)$ (in Y-coordinates), and linear fitting is applied to it as shown in Fig. 22(a-c). Crystallite size is determined from EQs. 2, and slope of the plot represents the lattice strain. Crystallite size and lattice strain for all samples is presented in Table 10. The copper peaks present in wire sample are not considered during evaluation of crystallite size and lattice strain, due to their very low intensities compared to ferrite peaks.

$$\Delta K = \frac{0.9}{D} + \Delta K_D$$

1

$$D = \frac{K \times \lambda}{I}$$

2

It has been observed from Table 10 that there is less variation in crystallite size between top and bottom surface of the deposits as compared to wire, which indicates a reduction in anisotropy. It is attributed to grain refinement in the bottom surface due to a relatively higher rate of cooling in bottom surface with respect to top surface. The lattice strain in both top and bottom layer is compressive in nature.

4.6.1. Dislocation density measurement

Dislocation density is also computed through X-ray diffraction method. It is computed using a modified Williamson hall plot [55–58]. In modified W-H plot, K is substituted by $KC^{1/2}$ as per EQs. 3–5 [57, 58]. Here a linear fit plot is prepared between ΔK and $KC^{1/2}$ (Fig. 23(a-c)), and the value of slope is determined to compute the dislocation density. The computed dislocation density for all samples is presented in Table 10. The graphical variation of crystallite size, lattice strain and dislocation density for all three samples is presented in Fig. 24.

$$\Delta K \cong \frac{0.9}{D} + \left[\left(\frac{\pi M^2 b^2}{2} \right) \times \rho^{\frac{1}{2}} \times \left(KC^{\frac{1}{2}} \right) \right] \pm \left[O \times \left(KC^{\frac{1}{2}} \right)^2 \right]$$

3

Where, $\Delta K = \frac{a \times \cos(\theta)}{\lambda}$ and $K = \frac{2 \sin(\theta)}{\lambda}$ (4)

By neglecting the higher terms $\left[O \times \left(KC^{\frac{1}{2}} \right)^2 \right]$ EQs. (2) becomes

$$\rho = \frac{2 \times \beta^2}{\pi M^2 b^2}$$

5

Where,

θ	Bragg's diffraction angle	b	Burger's vector (0.2485×10⁻⁹ m)
K	Scherer's constant	ρ	Dislocation density (1/m ²)
λ	Wavelength of the X-ray source	C	Contrast factor
I	Intercept of the linear fit plot between 4Sin(θ) and aCos(θ)	O	Higher-order component of KC ^{1/2}
D	Crystallite size	a	FWHM (full width half maximum)
M	Material constant varies between 1 and 2 M = 1 represents no deformation in the material M = 2 represents a material with deformations	β	Slope of linear fit plot between ΔK and KC ^{1/2}

Table 10
Crystallite size, lattice strain, and dislocation density of samples

Sample	Crystallite size (nm)	Lattice strain	Dislocation density (1/m ²)
Wire (ER70S-6)	23.04931507	0.000446959	3.2663×10 ¹³
Top Surface	18.38907104	-8.21E-04	3.8992×10 ¹²
Bottom Surface	16.27272727	-1.49E-03	7.3769×10 ¹³

Dislocation density observed in the deposits is more as compared to wire material, which means the strength of the deposits is better than that of wire. It has been observed that small crystallite size exhibits a larger dislocation density.

4.7. Residual stress measurement

Residual stress is measured using the XRD method through BRUKER D8-Advance®. In the XRD method, residual stress is computed by analysing the peak shifting phenomenon (as shown in Fig. 25). The standard d-Sin²(ψ) method is followed for calculating the value of residual stress present on the sample surface [59–64]. The procedure for residual stress calculation is based on the work reported in [59]. In d-Sin²(ψ) method, a graph (as shown in Fig. 26) is plotted between interplanar spacing (d) and Sin²(ψ), from which residual stress is computed [59–64]. For residual stress measurement, current and voltage are set at 40 mA and 40 KV respectively for performing initial 2θ scanning from 30° to 126° for all samples. In this 2θ range the observed diffraction peaks are {110}, {200}, {211}, and {220}. From the above planes, {211} plane is selected, which appeared at 99.6°, and residual stress is determined about this peak for all samples [60].

Here diffraction peaks are recorded at different ψ values (from -40° to 40°), and their corresponding interplanar spacing is determined. The obtained residual stress among the wire, top and bottom layer of the deposit is presented in Table 11 and Fig. 27.

Table 11
Residual stress value for wire, top, and bottom surface of the deposit

Sample	Residual stress (MPa)
Wire (ER70S-6)	-227.3 ± 7.9
Top Surface	100.8 ± 2.9
Bottom Surface	-139.1 ± 2.5

Residual stress observed in all three samples (from Table 11 and Fig. 27) is compressive in nature due to negative slope. As compared to wire, the magnitude of compressive residual stress is decreasing in the deposits, which means large residual stress present in the wire is relieved during the deposition process. Both top and bottom layer of the deposit exhibits compressive residual stress, which means through the NTA approach, compressive residual stress is developed in the fabricated part. As compared to previous kinds of literature without any external post-processing, tensile residual stress is present in the deposition, which reduces mechanical performance of the fabricated part [16, 18]. In the NTA process, a layer is fabricated through drop by drop transfer of molten metal, which act as a thermal load during the deposition process. Also, when a detached droplet starts to cool at that time, another droplet is deposited adjacent to the previous one. As a result, continuous cooling and heating cycle is going on during the deposition process. Therefore compressive residual stress is developed in the deposits. The development of compressive residual stress will further improve the mechanical performance of the fabricated part in terms of high strength and fatigue life [18]. Less variation of residual stress between top and bottom layer symbolises the isotropic nature of the deposit.

4.8. Microhardness analysis

Vickers microhardness tester is used to perform the microhardness analysis at 500 gf load, and 10s dwell time [16, 19]. Before conducting the microhardness test, the samples are polished to get a flat surface. Microhardness is measured in top, bottom and lateral surface of the deposit. Indentations are made on the central axis of deposit. For the top and bottom surface, a 5mm gap is provided between each indentation, but for the lateral surface, a 3mm gap is provided between each indentation from the top surface. Microhardness values in all three samples are presented in Table 12–13. The variation of microhardness value with increasing distance is presented in Fig. 28.

Table 12
Variation of microhardness in the top and bottom surface of the deposit

Distance (mm)	Microhardness in top surface (HV)	Microhardness in bottom surface (HV)
5	254.7	214.2
10	270.9	239.7
15	220.9	262.6
20	231.5	213
25	195.9	250.1
30	225.9	226.5
35	209.2	215.2
40	222.1	224.5
45	235	209.9
50	226.4	210.8
55	214.4	204.6
60	253.7	220.4
65	224	225.3
70	234.5	257.1
75	238.6	291.3
80	268.7	215
85	225.2	266
90	222.6	245.5
Average	231.9	232.872

Table 13
Variation of microhardness in the lateral surface of the deposit

Distance from top surface (mm)	Microhardness in lateral surface (HV)
3	226.7
6	224.3
9	238.9
12	232
15	204.1
18	203.3
21	206.7
24	224.4
27	231.3
30	241.5
33	261.7
Average	226.809

It has been observed from Table 12–13 and Fig. 28 that the average microhardness value corresponding to top, bottom, and lateral surface of the deposits is 231.9 HV, 232.872 HV, and 226.809 HV, respectively. The microhardness value is marginally more in the bottom layer with respect to top surface of the deposit. It is due to the grain refinement that occurred in the bottom surface of the deposit due to better cooling action. There is less variation in microhardness value in between lateral and longitudinal directions. Therefore it can be concluded that the NTA approach generates isotropic deposits.

5. Conclusions

NTA based WAAM has been successfully developed to fabricate deposits using ER70S-6 wire. Both single and multilayered deposits are fabricated through this approach, and the interaction of deposition parameters with response characteristics has been discussed. This investigation ends with the following conclusions.

- Due to no direct electrical arc contact with substrate, heat generated at the arcing zone is fully utilised to melt the wire electrode that enhances energy efficiency and deposition rate. It also facilitates deposits on non-conductive surfaces like SiO₂ for easy withdrawing of deposits after complete fabrication. This leads to a reduction in high substrate material wastage, cost and energy.
- From the GRA study, WFS and welding voltage is identified as key deposition parameter during multi-performance analysis for this NTA process. As it controls the heat input, droplet diameter and detachment frequency, over which bead geometry mostly depends.

- This approach not only reduces the heat input but also provides significant bead uniformity at minimal spatter and bead height difference between arc start and exit point of the arc.
- The microstructural analysis reveals complete ferrite concentration with few pearlites in both top, bottom, and interface surface of the deposits with almost similar elemental composition.
- XRD analysis reveals ferrite diffractions peaks [{110}, {200}, {211}, {220}] in wire, top and bottom surface, whereas some copper peaks [{111} and {200}] are also detected in wire surface. Dislocation density in the deposit is more with respect to wire material, which means strength of the deposits is better than that of wire.
- Compressive residual stress is noticed in the deposition, due to the application of thermal load during droplet detachment to substrate and due to continuous cooling and heating cycle in the NTA process. It will improve the mechanical performance of the fabricated part in terms of high strength and fatigue life.
- The average microhardness value corresponds to top, bottom, and lateral surface of the deposits is 231.9 HV, 232.872 HV, and 226.809 HV, respectively. Less variation in crystallite size, stress, strain and microhardness among top, bottom, and lateral surface of the deposit indicates isotropic nature of fabricated part.
- It is further recommended to study and perform the NTA process for getting better control over deposition parameters while maintaining good geometrical accuracy during fabrication of multi-layered components over non-conductive substrates.

Declarations

Funding *The authors declare that no funds, grants, or other support were received during the preparation of this manuscript.*

Competing interests *The authors declare no competing interests.*

Financial interests *The authors have no relevant financial or non-financial interests to disclose.*

Author contribution Process development, experimentation, analysis, and draft report was generated by Suvranshu Pattanayak. Susanta Kumar Sahoo guided the whole work and make necessary corrections to the draft report. Ananda Kumar Sahoo made corrections at some portions of the draft report. All authors read and approved the final manuscript.

References

1. Ding D, Pan Z, Cuiuri D, Li H (2015) Wire-feed additive manufacturing of metal components: technologies, developments and future interests. *Int J Adv Manuf Technol* 81:465-481. <https://doi.org/10.1007/s00170-015-7077-3>
2. Pattanayak S, Sahoo SK (2021) Gas metal arc welding based additive manufacturing—a review. *CIRP Journal of Manufacturing Science and Technology* 33:398–442.

<https://doi.org/10.1016/j.cirpj.2021.04.010>

3. Xiong J, Zhang G, Qiu Z, Li Y (2013) Vision-sensing and bead width control of a single-bead multilayer part: material and energy savings in GMAW-based rapid manufacturing. *Journal of Cleaner Production* 41:82-88. <https://doi.org/10.1016/j.jclepro.2012.10.009>
4. Xiong J, Zhang G (2014) Adaptive control of deposited height in GMAW-based layer additive manufacturing. *Journal of Materials Processing Technology* 214(4):962– 968. <https://doi.org/10.1016/j.jmatprotec.2013.11.014>
5. Xiong J, Yin Z, Zhang W (2016) Closed-loop control of variable layer width for thin-walled parts in wire and arc additive manufacturing. *Journal of Materials Processing Technology* 233:100–106. <https://doi.org/10.1016/j.jmatprotec.2016.02.021>
6. Xiong J, Yin Z, Zhang W (2016) Forming appearance control of arc striking and extinguishing area in multilayer single-pass GMAW-based additive manufacturing. *Int J Adv Manuf Technol* 87:579–586. <https://doi.org/10.1007/s00170-016-8543-2>
7. Cunningham CR, Flynn JM, Shokrani A, Dhokia V, Newman ST (2018) Invited review article: Strategies and processes for high quality wire arc additive manufacturing. *Additive Manufacturing* 22:672–686. <https://doi.org/10.1016/j.addma.2018.06.020>
8. Wu B, Pan Z, Ding D, Cuiuri D, Li H, Xu J, Norrish J (2018) A review of the wire arc additive manufacturing of metals: properties, defects and quality improvement. *Journal of Manufacturing Processes* 35:127–139. <https://doi.org/10.1016/j.jmapro.2018.08.001>
9. Majeed A, Ahmed A, Lv J, Peng T, Muzamil M (2020) A state-of-the-art review on energy consumption and quality characteristics in metal additive manufacturing processes. *J Braz. Soc. Mech. Sci. Eng.* 42:249. <https://doi.org/10.1007/s40430-020-02323-4>
10. Song YA, Park S, Choi D, Jee H (2005) 3D welding and milling: Part I—a direct approach for freeform fabrication of metallic prototypes. *International Journal of Machine Tools & Manufacture* 45:1057–1062. <https://doi.org/10.1016/j.ijmactools.2004.11.021>
11. Song YA, Park S (2006) Experimental investigations into rapid prototyping of composites by novel hybrid deposition process. *Journal of Materials Processing Technology* 171(1):35–40. <https://doi.org/10.1016/j.jmatprotec.2005.06.062>
12. Suryakumar S, Karunakaran KP, Bernard A, Chandrasekhar U, Raghavender N, Sharma D (2011) Weld bead modeling and process optimisation in Hybrid Layered Manufacturing. *Computer-Aided Design* 43(4):331–344. <https://doi.org/10.1016/j.cad.2011.01.006>
13. Cao Y, Zhu S, Liang X, Wang W (2011) Overlapping model of beads and curve fitting of bead section for rapid manufacturing by robotic MAG welding process. *Robotics and Computer-Integrated Manufacturing* 27(3):641–645. <https://doi.org/10.1016/j.rcim.2010.11.002>
14. Xiong J, Zhang G, Gao H, Wu L (2013) Modeling of bead section profile and overlapping beads with experimental validation for robotic GMAW-based rapid manufacturing. *Robotics and Computer-Integrated Manufacturing* 29(2):417–423. <https://doi.org/10.1016/j.rcim.2012.09.011>
15. Li Y, Han Q, Zhang G, Horvath I (2018) A layers-overlapping strategy for robotic wire and arc additive manufacturing of multilayer multi-bead components with homogeneous layers. *Int J Adv Manuf*

- Technol 96:3331–3344. <https://doi.org/10.1007/s00170-018-1786-3>
16. Colegrove PA, Coules HE, Fairman J, Martina F, Kashoob T, Mamash H, Cozzolino LD (2013) Microstructure and residual stress improvement in wire and arc additively manufactured parts through high-pressure rolling. *Journal of Materials Processing Technology* 213:1782–1791. <https://doi.org/10.1016/j.jmatprotec.2013.04.012>
 17. Xie Y, Zhang H, Zhou F (2016) Improvement in geometrical accuracy and mechanical property for arc-based additive manufacturing using metamorphic rolling mechanism. *Manuf. Sci. Eng.* 138(11):111022. <https://doi.org/10.1115/1.4032079>
 18. Dirisu P, Supriyo G, Martina F, Xu X, Williams S (2020) Wire plus arc additive manufactured functional steel surfaces enhanced by rolling. *International Journal of Fatigue* 130:105237. <https://doi.org/10.1016/j.ijfatigue.2019.105237>
 19. Somashekara M, Adinarayanappa, Simhambhatla S (2018) Twin-wire welding based additive manufacturing (TWAM): manufacture of functionally gradient objects. *Rapid Prototyping Journal* 23(5):858–868. <https://doi.org/10.1108/RPJ-09-2015-0126>
 20. Abe T, Mori D, Sonoya K, Nakamura M, Sasahara H (2019) Control of the chemical composition distribution in deposited metal by wire and arc-based additive manufacturing. *Precision Engineering* 55:231–239. <https://doi.org/10.1016/j.precisioneng.2018.09.010>
 21. Liu K, Chen X, Shen Q, Pan Z, Singh RA, Jayalakshmi S, Konovalov S (2020) Microstructural evolution and mechanical properties of deep cryogenic treated Cu–Al–Si alloy fabricated by Cold Metal Transfer (CMT) process. *Materials Characterization* 159:110011. <https://doi.org/10.1016/j.matchar.2019.110011>
 22. Yang D, He C, Zhang G (2016) Forming characteristics of thin-wall steel parts by double electrode GMAW based additive manufacturing. *Journal of Materials Processing Technology* 227:153–160. <https://doi.org/10.1016/j.jmatprotec.2015.08.021>
 23. Yang D, Wang G, Zhang G (2017) A comparative study of GMAW- and DE-GMAW-based additive manufacturing techniques: thermal behavior of the deposition process for thin-walled parts. *Int J Adv Manuf Technol* 91:2175–2184. <https://doi.org/10.1007/s00170-016-9898-0>
 24. Guo M, Jia C, Zhou J, Liu W, Wu C (2020) Investigating the generation process of molten droplets and arc plasma in the confined space during compulsively constricted WAAM. *Journal of Materials Processing Technology* 275:116355. <https://doi.org/10.1016/j.jmatprotec.2019.116355>
 25. Jia C, Liu W, Chen M, Guo M, Wu S, Wu C (2020) Investigation on arc plasma, droplet, and molten pool behaviours in compulsively constricted WAAM. *Additive Manufacturing* 34:101235. <https://doi.org/10.1016/j.addma.2020.101235>
 26. Liu W, Jia C, Guo M, Gao J, Wu C (2019) Compulsively constricted WAAM with arc plasma and droplets ejected from a narrow space. *Additive Manufacturing* 27:109–117. <https://doi.org/10.1016/j.addma.2019.03.003>
 27. Zhou J, Jia C, Guo M, Chen M, Gao J, Wu C (2021) Investigation of the WAAM processes features based on an indirect arc between two non-consumable electrodes. *Vacuum* 183:109851. <https://doi.org/10.1016/j.vacuum.2020.109851>

28. Deng JL (1989) Introduction to grey system theory, *The Journal of Grey System* 1(1):1–24.
29. Pattanayak S, Panda S, Dhupal D (2020) Laser micro drilling of 316L stainless steel orthopedic implant: A study. *Journal of Manufacturing Processes* 52:220-234.
<https://doi.org/10.1016/j.jmapro.2020.01.042>
30. Little RL (1973) *Welding and Welding Technology*. New York, McGraw Hill.
31. Conner LP (1987) *Welding Handbook*. 8th edition Welding Technology. American Welding Society, USA.
32. Kah P, Latifi H, Suoranta R, Martikainen J, Pirinen M (2014) Usability of arc types in industrial welding. *Int J Mech Mater Eng*. 9(15). <http://dx.doi.org/10.1186/s40712-014-0015-6>
33. Nie Y, Zhang P, Wu X, Li G, Yan H, Yu Z (2018) Rapid prototyping of 4043 al-alloy parts by cold metal transfer. *Science and Technology of Welding and Joining* 23(6):527–535.
<http://dx.doi.org/10.1080/13621718.2018.1438236>
34. Baby J, Amirthalingam M (2020) Microstructural development during wire arc additive manufacturing of copper-based components. *Weld World* 64:395–405. <http://dx.doi.org/10.1007/s40194-019-00840-y>
35. Gou J, Wang Z, Hua S, Shen J, Tian Y, Zhao G, Chen Y (2020) Effects of ultrasonic peening treatment in three directions on grain refinement and anisotropy of cold metal transfer additive manufactured ti-6al-4v thin wall structure. *Journal of Manufacturing Processes* 54:148–157.
<https://doi.org/10.1016/j.jmapro.2020.03.010>
36. Yuan L, Pan Z, Ding D, Yu Z, Duin SV, Li H, Li W, Norrish J (2020) Fabrication of metallic parts with overhanging structures using the robotic wire arc additive manufacturing. *Journal of Manufacturing Processes* 63:24-34. [http:// dx.doi.org/10.1016/j.jmapro.2020.03.018](http://dx.doi.org/10.1016/j.jmapro.2020.03.018)
37. Yuan L, Pan Z, Ding D, He F, Duin SV, Li H, Li W (2020) Investigation of humping phenomenon for the multi-directional robotic wire and arc additive manufacturing. *Robotics and Computer Integrated Manufacturing* 63:101916. <http://dx.doi.org/10.1016/j.rcim.2019.101916>
38. Liang Z, Yi L, Jingtao H, Chengyang Z, Jie X, Dong C (2019) Energy characteristics of droplet transfer in wire-arc additive manufacturing based on the analysis of arc signals. *Measurement* 134:804–813.
<https://doi.org/10.1016/j.measurement.2018.10.048>
39. Yili D, Shengfu Y, Yusheng S, Tianying H, Lichao Z (2018) Wire and arc additive manufacture of high-building multi-directional pipe joint. *Int J Adv Manuf Technol* 96:2389–2396.
<https://doi.org/10.1007/s00170-018-1742-2>
40. Ou W, Mukherjee T, Knapp GL, Wei Y, Roy TD (2018) Fusion zone geometries, cooling rates and solidification parameters during wire arc additive manufacturing. *International Journal of Heat and Mass Transfer* 127 part-c:1084–1094. <https://doi.org/10.1016/j.ijheatmasstransfer.2018.08.111>
41. Hu Z, Qin X, Shao T, Liu H (2018) Understanding and Overcoming of Abnormality at Start and End of the Weld Bead in Additive Manufacturing With GMAW. *Int J Adv Manuf Technol* 95:2357–2368.
<https://doi.org/10.1007/s00170-017-1392-9>
42. Wang Z, Chevret SZ, Leonard F, Abba G (2022) Improvement strategy for the geometric accuracy of bead's beginning and end parts in wire-arc additive manufacturing (WAAM). *Int J Adv Manuf Technol* 118:2139–2151. <https://doi.org/10.1007/s00170-021-08037-8>

43. Yildiz AS, Davut K, Koc B, Yilmaz O (2020) Wire arc additive manufacturing of high-strength low alloy steels: study of process parameters and their influence on the bead geometry and mechanical characteristics. *Int J Adv Manuf Technol* 108:3391–3404. <https://doi.org/10.1007/s00170-020-05482-9>
44. Su C, Chen X, Gao C, Wang Y (2019) Effect of heat input on microstructure and mechanical properties of al-mg alloys fabricated by WAAM. *Applied Surface Science* 486:431–440. <https://doi.org/10.1016/j.apsusc.2019.04.255>
45. Cadiou S, Courtois M, Carin M, Berckmans W, Masson PL (2020) Heat transfer, fluid flow and electromagnetic model of droplets generation and melt pool behaviour for wire arc additive manufacturing. *International Journal of Heat and Mass Transfer* 148 (2020), 119102. <http://dx.doi.org/10.1016/j.ijheatmasstransfer.2019.119102>
46. Yamaguchi M, Komata R, Furumoto T, Abe S, Hosokawa A (2022) Influence of metal transfer behavior under Ar and CO₂ shielding gases on geometry and surface roughness of single and multilayer structures in GMAW-based wire arc additive manufacturing of mild steel. *Int J Adv Manuf Technol* 119:911–926. <https://doi.org/10.1007/s00170-021-08231-8>
47. Rafieezad M, Ghaffari M, Nemani AV, Nasiri A (2019) Microstructural evolution and mechanical properties of a low-carbon low-alloy steel produced by wire arc additive manufacturing. *Int J Adv Manuf Technol* 105:2121–2134. <https://doi.org/10.1007/s00170-019-04393-8>
48. Nemani AV, Ghaffari M, Nasiri A (2020) Comparison of microstructural characteristics and mechanical properties of shipbuilding steel plates fabricated by conventional rolling versus wire arc additive manufacturing. *Additive Manufacturing*, 32:101086. <http://dx.doi.org/10.1016/j.addma.2020.101086>
49. Van D, Dinda GP, Park J, Mazumder J, Lee SH (2020) Enhancing hardness of Inconel 718 deposits using the aging effects of cold metal transfer-based additive manufacturing. *Materials Science & Engineering: A* 776:139005. <https://doi.org/10.1016/j.msea.2020.139005>
50. Embury D (2012) The formation of pearlite in steels. Editor(s): Elena Pereloma, David V. Edmonds, In *Woodhead Publishing Series in Metals and Surface Engineering, Phase Transformations in Steels*, Woodhead Publishing, 1, pp. 276-310. ISBN 9781845699703. <https://doi.org/10.1533/9780857096104.2.276>
51. Ke WC, Oliveira JP, Cong BQ, Ao SS, Qi ZW, Peng B, Zeng Z (2022) Multi-layer deposition mechanism in ultra high-frequency pulsed wire arc additive manufacturing (WAAM) of NiTi shape memory alloys. *Additive Manufacturing* 50:102513. <https://doi.org/10.1016/j.addma.2021.102513>
52. Swanson HE, Gilfrich NT, Ugrinic GM (1955) *Natl. Bur. Stand. (U.S.), Circ.*, 539 5, 22.
53. Jung Z (1926) *Kristallogr. Kristallgeom., Kristallphys., Kristallchem.*, 64(419).
54. Kumar S, Ohlan A, Kumar P, Verma V (2020) Improved Electromagnetic Interference Shielding Response of Polyaniline Containing Magnetic Nano-ferrites. *Journal of Superconductivity and Novel Magnetism* 33:1187–1198. <https://doi.org/10.1007/s10948-019-05343-x>
55. Dutta K, Mishra SK, Dwivedi PK, Sivateja C (2021) On the characteristic features of dislocations during ratcheting–creep interaction. *J. of Materi Eng and Perform* 30:7376–7385. <https://doi.org/10.1007/s11665-021-05934-7>

56. Janardhan G, Kishore K, Dutta K, Mukhopadhyay G (2020) Tensile and fatigue behavior of resistance spot welded HSLA steel sheets: Effect of pre-strain in association with dislocation density. *Materials Science & Engineering: A* 793:139796. <https://doi.org/10.1016/j.msea.2020.139796>
57. Ungar T, Leoni M, Scardi P (1999) The dislocation model of strain anisotropy in whole powder-pattern fitting: the case of an Li–Mn cubic spinel. *J. Appl. Crystallogr* 32:290–295. <https://doi.org/10.1107/S0021889898012710>.
58. Kishor R, Sahu L, Dutta K, Mondal AK (2014) Assessment of dislocation density in asymmetrically cyclic loaded non-conventional stainless steel using X-ray diffraction profile analysis. *Materials Science & Engineering: A* 598:299–303. <https://doi.org/10.1016/j.msea.2014.01.043>
59. Prevey PS (1986) X-ray Diffraction Residual Stress Techniques. *Metals Handbook*. 10, Metals Park: American Society for Metals pp. 380-392.
60. Ruud CO, DiMascio PS, Yavelak JJ (1985) Comparison of three residual-stress measurement methods on a mild steel bar. *Experimental Mechanics*, vol. 25:338–343. <https://doi.org/10.1007/BF02321331>
61. Murray C, Noyan IC (2013) Applied and residual stress determination using x-ray diffraction, in *practical residual stress measurement methods*. Vancouver, University of British Columbia pp. 139-161. <https://doi.org/10.1002/9781118402832.ch6>
62. Cullity BD (1978) *Elements of x-ray diffraction*. 2nd ed., Addison-Wesley Publishing Company, Inc., Menlo Park pp. 451–465.
63. Pineault JA, Belassel M, Brauss ME (2002) X-Ray diffraction residual stress measurement in failure analysis. *ASM handbook, Failure analysis and prevention*, R.J. Shipley and W.T. Becker, Ed., ASM International, Materials Park 11:484–485.
64. Ganesh P, Rai AK, Dwivedi PK, Chowdhury A, Biswal R, Nagpure DC, Sundar R, Gupta RK, Ranganathan K, Bindra KS, Kaul R (2019) Study on Enhancing Fatigue Life of SAE 9260 Spring Steel with Surface Defect Through Laser Shock Peening. *J. of Materi Eng and Perform* 28:2029–2035. <https://doi.org/10.1007/s11665-019-03990-8>

Figures

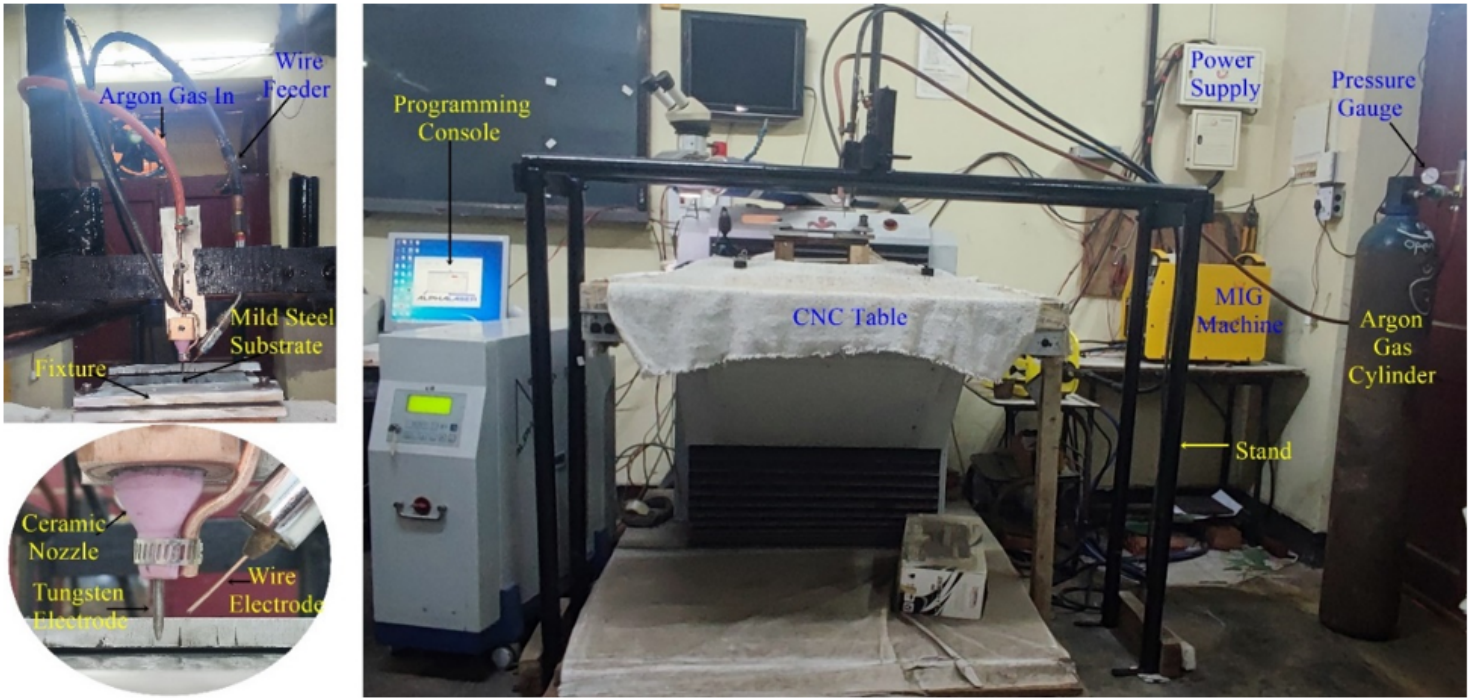


Figure 1

Experimental setup of NTA based WAAM

Figure 2

(a) Electrode holder and gas supply system, (b) droplet detachment process

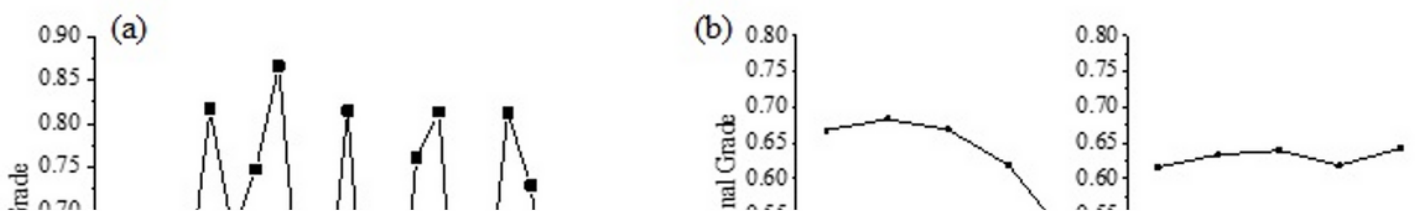


Figure 3

Grey relational grade corresponds to (a) each experimental trials, (b) each deposition parameter levels



Figure 4

Beads deposited with different parameter sets

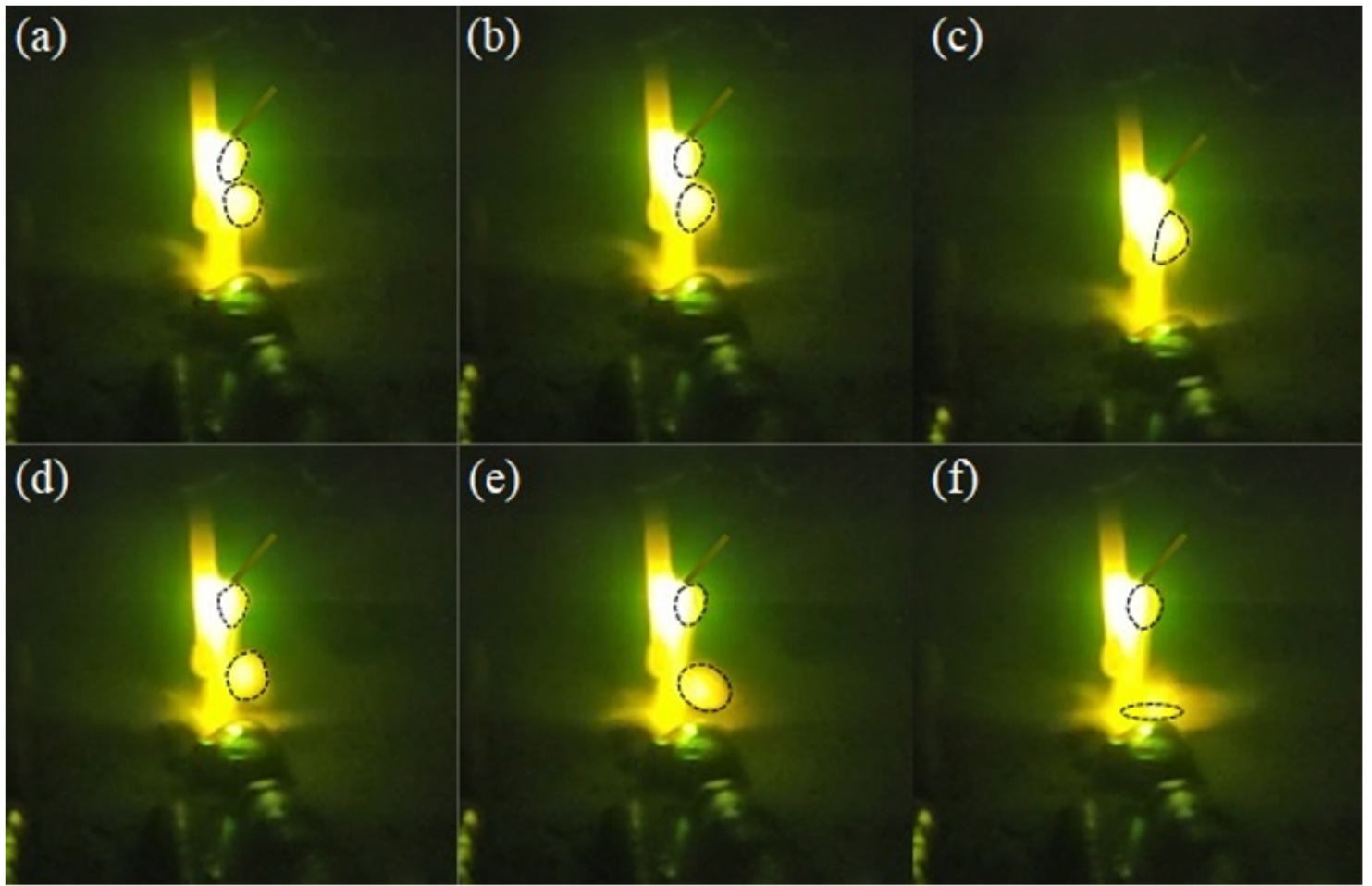


Figure 5

Process of droplet transfer at 'A₂, B₅, C₁, and D₅' parametric combination

Figure 6

Deposition made over SiO₂ substrate (a) single-layered, (b) multi-layered

Figure 7

Parametric influence on bead width deviation and height difference

Figure 8

Parametric effect of welding voltage and WFS on bead width deviation

Figure 9

Role of welding voltage on wear and diffusion of tungsten electrode

Figure 10

Parametric effect of welding voltage and current on bead height deviation

Figure 11

Parametric influences on droplet diameter and detachment frequency

Figure 12

Parametric interaction of welding current and WFS with droplet diameter

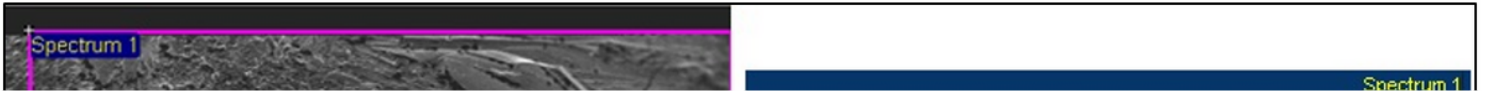


Figure 13

EDS report of tungsten electrode surface at a low level of welding current

Figure 14

Concentric plasma jet under high WFS

Figure 15

Parametric influence of WFS and welding voltage on droplet detachment frequency

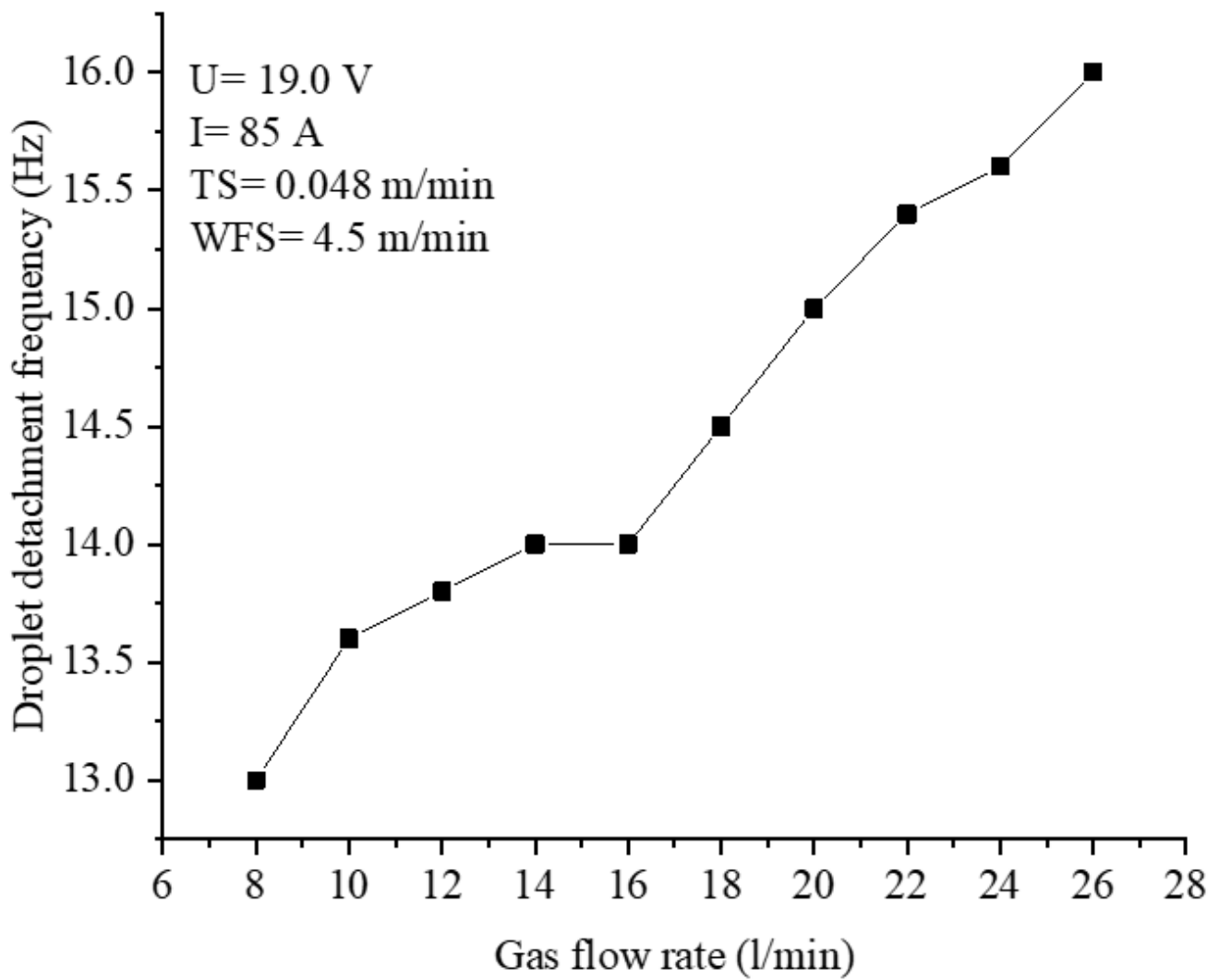


Figure 16

Impact of gas flow rate on droplet detachment frequency

Figure 17

Contamination of tungsten electrode in absence of shielding gas

Figure 18

Microstructural evolution on (a) top surface, (b) bottom surface, (c) interface layer, (d) enlarged view of top, (e) enlarged view of bottom, (f) enlarged view of interface

Figure 19

Microstructure of the droplet forms at wire tip after deposition of a layer

Figure 20

EDS result of (a) wire, (b) top surface, (c) bottom surface, (d) interface

Figure 21

Diffraction patterns of wire, top and bottom surface

Figure 22

W-H plot of (a) ER70S6 wire, (b) top surface, (c) bottom surface

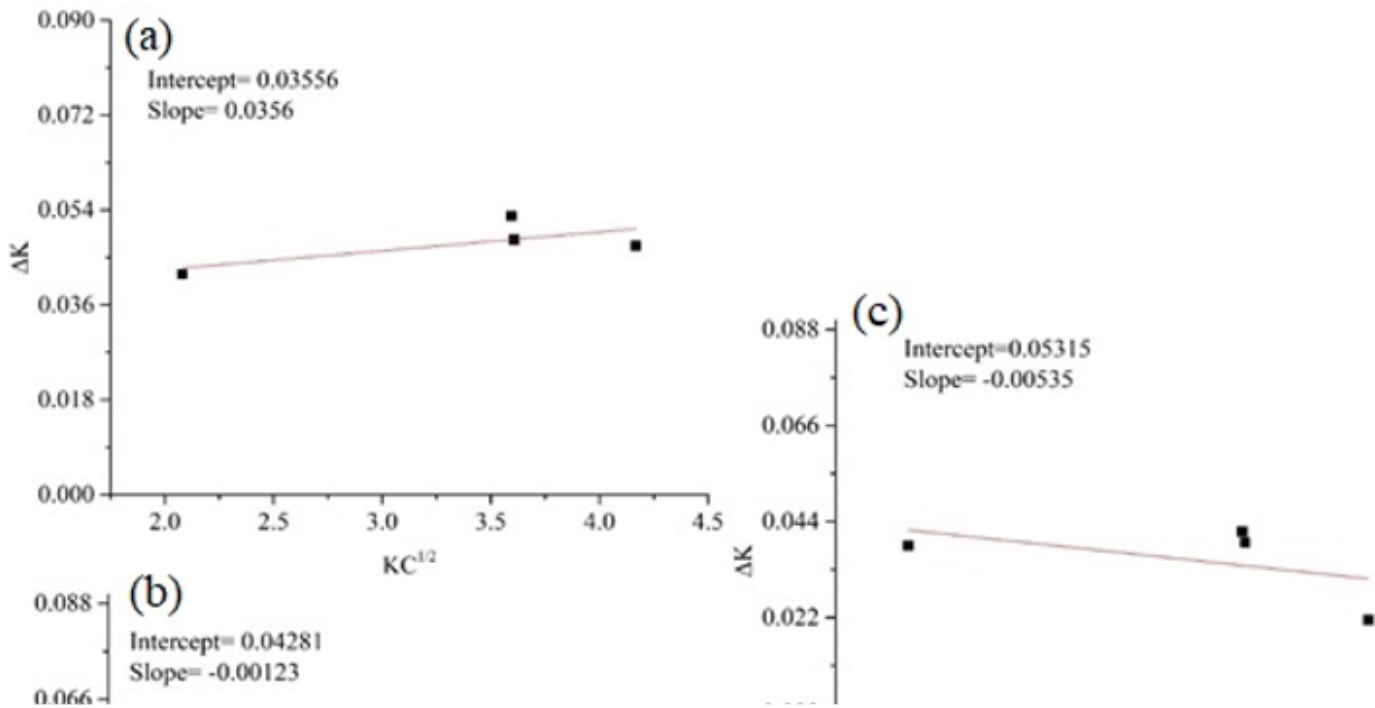


Figure 23

Modified W-H plot for (a) ER70S6 wire, (b) top surface, (c) bottom surface

Figure 24

Variation of (a) crystallite size, (b) lattice strain, and (c) dislocation density among wire and deposits

Figure 25

Peak shifting phenomenon during the presence of residual stress

Figure 26

d-Sin²(ψ) plot for (a) wire, (b) top, (c) bottom surface of deposit

Figure 27

Residual stress variation among wire, top and bottom layer of the deposit

Figure 28

Variation of microhardness between (a) longitudinal, (b) lateral surface of deposit